Photodissociation of dicarbon: How nature breaks an unusual multiple bond

Jasmin Borsovszky[a], Klaas Nauta[a], Jun Jiang[b], Christopher S. Hansen[a], Laura K. McKemmish[a], Robert W. Field[c], John F. Stanton[d], Scott H. Kable[a,1], and Timothy W. Schmidt[a,1]

[a]School of Chemistry, University of New South Wales, Sydney, NSW 2052, Australia; [b]Center for Accelerator Mass Spectrometry, Lawrence Livermore National Laboratory, Livermore, CA 94550; [c]Department of Chemistry, Massachussetts Institute of Technology, Cambridge, MA 02139; and [d]Department of Chemistry, University of Florida, Gainesville, FL 32611

Edited by Daniel Neumark, Department of Chemistry, University of California, Berkeley, CA; received July 21, 2021; approved October 25, 2021

The dicarbon molecule (C_2) is found in flames, comets, stars, and the diffuse interstellar medium. In comets, it is responsible for the green color of the coma, but it is not found in the tail. It has long been held to photodissociate in sunlight with a lifetime precluding observation in the tail, but the mechanism was not known. Here we directly observe photodissociation of C_2. From the speed of the recoiling carbon atoms, a bond dissociation energy of 602.804(29) kJ·mol^{-1} is determined, with an uncertainty comparable to its more experimentally accessible N_2 and O_2 counterparts. The value is within 0.03 kJ·mol^{-1} of high-level quantum theory. This work shows that, to break the quadruple bond of C_2 using sunlight, the molecule must absorb two photons and undergo two "forbidden" transitions.

comets | dicarbon | photodissociation

Alongside N_2 and O_2, C_2 is a fundamental homonuclear diatomic molecule (1). As a simple molecule, it should be a foundation stone of bonding theories. Yet, its electronic structure defies description by a single electronic configuration (2–4). It is more amenable to a description by valence bond theory whereby it is found to exhibit a triple bond as in N_2, but with the outer electrons forming a fourth bond of the Heitler–London type (5). This interpretation is not without controversy (3, 6–10) but is supported by detailed inspection of the many-electron wavefunction (11).

Unlike its atmospheric counterparts, C_2 exists only in rarefied or energetic environments, owing to its reactivity. It is found in carbon stars and the interstellar medium (12–15). It is also of great importance in combustion (16). In its lowest triplet state, C_2 announces its presence in flames and comets as blue-green fluorescence: the Swan bands ($d^3\Pi_g \rightarrow a^3\Pi_u$; Fig. 1) (17, 18). The Swan bands were first reported as the origin of the green hue of cometary comae in 1868 (19). In the 1930s, it was suggested that excitation to the newly discovered $e^3\Pi_g$ state would result in photodissociation, thereby explaining why the coma of a comet was green but the tail was not (20). Empirically, astronomers place a lifetime on cometary C_2 of 10^5 s at 1 AU (21, 22). However, the photodissociation process has never been directly observed.

An observation of the photodissociation of C_2 would afford a measurement of its bond dissociation energy (BDE) to spectroscopic accuracy. The uncertainties of the BDEs of O_2 and N_2 are less than a few reciprocal centimeters (1 cm^{-1} = 0.012 kJ·mol^{-1}), and yet that for C_2 is an order of magnitude higher. Furthermore, the tabulated BDE of C_2 (23) relies heavily on the theoretical determination of Karton (24).

In the course of revising the spectroscopy of the Fox–Herzberg system of C_2 ($e^3\Pi_g - a^3\Pi_u$), we determined that the $v = 12$ level was likely predissociated (25). Predissociation occurs when a bound level is above the lowest dissociation energy and accesses the continuum by nonadiabatic coupling, in this case to the isosymmetric $d^3\Pi_g$ state. The mechanism is depicted in Fig. 1.

In this work, we image the carbon atom products of the photodissociation of C_2, proving the mechanism by which it is destroyed by sunlight in comets. The determined BDE is 602.804(29) kJ·mol^{-1} (50,390.5 ± 2.4 cm^{-1}). From this mechanism, we employ high level ab initio quantum chemical calculations to predict the lifetime of cometary C_2 as 1.6×10^5 s (∼2 d at 1 AU), consistent with astronomical observations.

Results

As opposed to our earlier work, where an electric discharge was used (25–31), C_2 is here produced by photolysis of C_2Cl_4, roughly 1 mm in front of the orifice of the nozzle producing the molecular beam. This was done to minimize the production of carbon atoms at the molecular beam source (32). C_2 is cooled by a free-jet expansion and is resonantly excited to $e^3\Pi_g(v = 12)$ at 201.5 nm. Some of the excited C_2 subsequently dissociates, while some C_2 absorbs a second pump photon to produce C_2^+, allowing us to monitor and optimize the C_2 production from its resonant two-photon ionization (R2PI) signal. The nascent carbon atoms are probed with a third laser by (2+1) resonance-enhanced multiphoton ionization (REMPI) (33). Carbon has three closely spaced spin–orbit components in the ^3P_J electronic ground state, $J = |L + S| = 2$, 1, and 0, with $J = 0$ as the lowest in energy. The three components and their energies are given in Table 1. Each of these three states can be individually probed by ionizing at a distinct wavelength.

Significance

It has long been observed that the coma of a comet is often green while its tail is not. While the explanation for this must be that the molecules responsible for the green emission, C_2, are photodissociated, the mechanism was, until now, unknown. We have observed the photodissociation of C_2 in the laboratory for the first time and, in doing so, have determined its bond dissociation energy with unprecedented precision. Invoking the observed mechanism, the calculated lifetime of cometary C_2 is found to be consistent with astronomical observations.

Author contributions: L.K.M., S.H.K., and T.W.S. designed research; J.B., K.N., J.J., C.S.H., R.W.F., J.F.S., and T.W.S. performed research; J.B., K.N., J.J., S.H.K., and T.W.S. analyzed data; and J.B., K.N., and T.W.S. wrote the paper.

The authors declare no competing interest.

This article is a PNAS Direct Submission.

[1]To whom correspondence may be addressed. Email: s.kable@unsw.edu.au or timothy.schmidt@unsw.edu.au.

This article contains supporting information online at https://www.pnas.org/lookup/suppl/doi:10.1073/pnas.2113315118/-/DCSupplemental.

Published December 20, 2021.

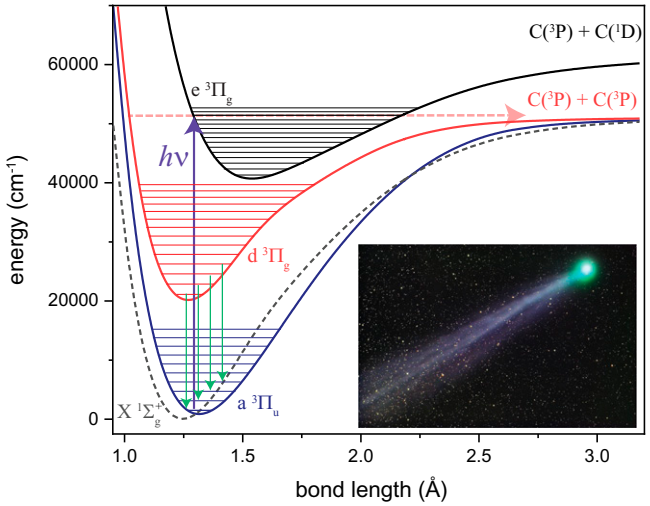

Fig. 1. States of C_2 involved in this study. We excite C_2 from the $v = 0$ level of the lowest triplet state, $a^3\Pi_u$, to the $v = 12$ level of the $e^3\Pi_g$ state (Fox–Herzberg bands). The level is predissociated, accessing the continuum on the $d^3\Pi_g$ state, where we probe the ^{3}P carbon atoms by resonant 2+1 photon ionization. The green fluorescence of C_2 in comets is due to $d^3\Pi_g \rightarrow a^3\Pi_u$ emission (Swan bands). *Inset*: Comet Lovejoy exhibiting strong Swan band emission in the coma. Image credit: John Vermette (photographer).

Fig. 2*A* shows an image of carbon atoms produced by exciting C_2 at 49,864.2 cm^{-1}, corresponding to the $Q_{31}(2)$ transition in the $(12 - 0)$ Fox–Herzberg band. A section of the spectrum of this band is shown in Fig. 2*B*; the assignments of the spectrum will be briefly discussed further below but essentially follow the assignments made previously (25). A larger portion of the $(12 - 0)$ band is shown and briefly discussed in *SI Appendix*. The two halves of the image in Fig. 2*A* are the "raw" image on the left and a three-dimensional (3D) slice reconstructed by the rBasex package on the right (34). The image was recorded by probing only the $^3P_2$ state of carbon.

Superficially, the image shows two distinct components: a diffuse background spread over the entire image and a bright central component. Upon closer inspection, the central component has, itself, a very tight central core only a few pixels wide, surrounded by a wider circle of up to 40 pixels radius. It is the broader central component that constitutes the true carbon signal resulting from dissociation of photoexcited C_2 molecules. The tight, bright core is a small amount of neutral atomic carbon produced at the nozzle tip, which is collisionally cooled and travels with the molecular beam and has therefore essentially no transverse velocity. The diffuse, high-speed background is attributed to carbon atoms, produced by the pump laser from leftover precursor molecules in the molecular beam, resonantly ionized by the probe laser. It is present regardless of whether the pump laser is resonant with a C_2 transition and was minimized by keeping the pump laser power density low. As shown in Fig. 2*B*, the spectrum obtained by monitoring the C_2 photofragments (photofragment excitation, PhoFEx) closely matches the observed C_2 R2PI spectrum, and a simulation of the $(12 - 0)$ Fox–Herzberg band using published spectroscopic constants (31). This allays any doubt that the observed ring of carbon atom fragments is due to dissociation of $v = 12$ $e^3\Pi_g$ state C_2 molecules.

Table 1. Atomic carbon energy levels

State	Energy cm^{-1}*	Atom pair (*J*, *J*)	Energy cm^{-1}
$^3P_0$	0	(0,0)	0
$^3P_1$	16.417	(0,1)/(0,1)	16.417
$^3P_2$	43.413	(1,1)	32.833
		(2,0)/(0,2)	43.413
		(2,1)/ (2,1)	59.830
		(2,2)	86.827

*Haris and Kramida (35).

The speed distribution of atomic carbon is obtained from the Abel-transformed image. Fig. 2*C* shows the distributions obtained by monitoring the $^3P_2$, $^3P_1$, and $^3P_0$ states of carbon. These three carbon states can be probed uniquely by tuning the probe laser to 280.340, 280.314, and 280.298 nm, respectively, by employing a (2+1) REMPI scheme with $\Delta J = 0$ transitions using the C(^{3}P) state at 71,300 cm^{-1} as an intermediate (35). The figure includes three backgrounds, recorded for each of the three carbon states by detuning the C_2 excitation laser from the resonant wavelength. The backgrounds clearly show that only the speed component between ~100 to 250 m·s^{-1} originates from the dissociation of resonantly excited C_2. The raw images are contained in *SI Appendix*.

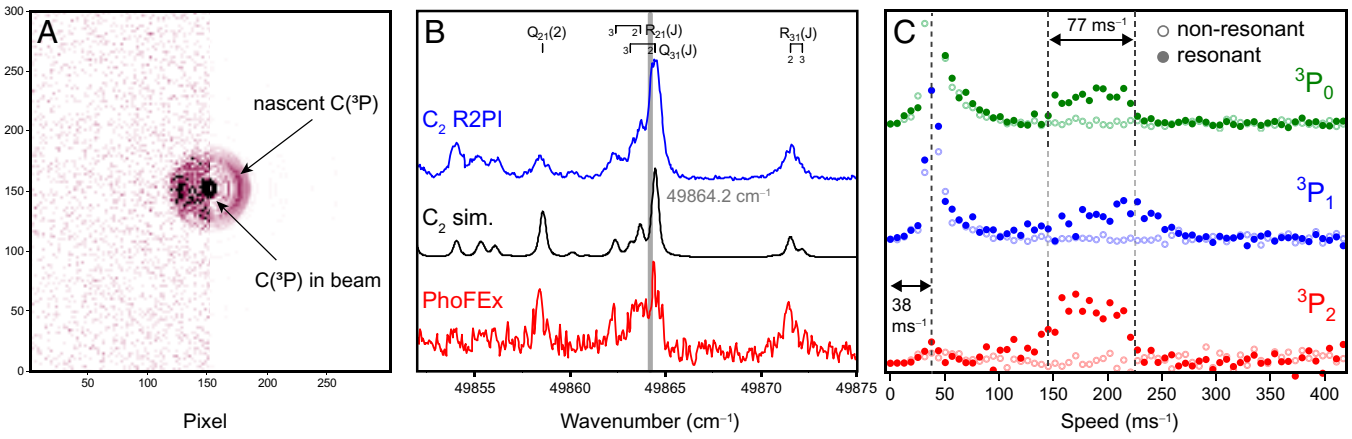

Fig. 2. (*A*) Velocity-mapped image of the $^3P_2$ state of carbon produced by photolyzing C_2 at 49,864.2 cm^{-1}. The two halves of the image are the "raw" image on the left and a 3D slice reconstructed by the rBasex method on the right (34). (*B*) Averaged photofragment excitation action (PhoFEx) spectrum of the $(12 - 0)$ band (*Bottom*) overlayed with the corresponding C_2 resonant 2-photon ionization (R2PI) spectrum (*Top*) and a simulation illustrating the band structure (*Middle*). These plots demonstrate conclusively that the nascent C(^{3}P) is generated by dissociation of $e^3\Pi_g$ $(v = 12)$ C_2. (*C*) The three speed distributions in meters per second resulting from the photodissociation of C_2 at 49,864.2 cm^{-1}. The three distributions were measured probing the $^3P_0$ (*Top*, green), $^3P_1$ (*Middle*, blue), and $^3P_2$ (*Bottom*, red) states of carbon. The nonresonant distributions are given as open symbols. The vertical dashed lines show the extent of signal broadening due to electron recoil.

The very cold component at the core of the image is located at a velocity of 38 m·s^{-1}. As this component results from carbon produced at the nozzle and therefore embedded in the molecular beam, the velocity offset from 0 m·s^{-1} needs to be explained. This velocity component arises from the excess ionization energy, manifest as velocity in the recoiling electron–ion pair. From the known ionization energy of C (35), the recoil velocity of the ion is 38.45 m·s^{-1}. The difference in recoil velocity for each spin–orbit state is about 0.1 m·s^{-1}, which is within the experimental resolution.

The width of the peak at 38 m·s^{-1} is due to residual transverse velocity in the molecular beam and space-charging effects. It is interesting to note that the intensity of the cold carbon peak at 38 m·s^{-1} is highest for the $^3P_0$ component and weakest for $^3P_2$. We attribute this to collisional cooling in the expansion at the nozzle tip, and the observed intensity ratio of the three carbon spin–orbit states is consistent with a 15 to 20 K molecular beam temperature. Analysis of this cold component reveals an anisotropy of $\beta \approx 0.4$. Detail of this region is shown in *SI Appendix*.

The ionization-induced velocity component explains the width observed in the speed distributions of the photofragments of C_2. Even a single, sharp velocity component from the photodissociation event will have a velocity spread of ± 38 m·s^{-1}, which is most clearly seen in the distributions measured for the $^3P_0$ and $^3P_2$ states of carbon, which closely resemble each other. The appearance of the speed distributions is explained in detail in *SI Appendix*. The image due to $^3P_2$ carbon from C_2 exhibits some anisotropy, characterized by $\beta \approx -0.5$.

The three ground states of carbon atom potentially result in six distinct product pair states as listed in Table 1. The dashed vertical lines in Fig. 2*C* make it clear that the distribution seen for the $^3P_0$ component matches the velocity distribution of $^3P_2$. That two components are closely momentum matched implies they belong to the same ($^3P_{J_1}$,$^3P_{J_2}$) product state. Moreover, the width of that component is 77 m·s^{-1}, which is the width expected for a single product state. We therefore assign the $^3P_0$ and $^3P_2$ distributions to the observation of the (0,2)/(2,0) atom pair. Knowing its identity, the center of this velocity component yields a value for the dissociation energy of C_2.

An accurate determination of this dissociation energy requires detailed modeling of the instrumental width function and the ionization-induced width. Each carbon atom ionizes at a very well-defined excess energy. This energy is slightly different for each of the three carbon states, but this difference, < 0.1 m·s^{-1}, is too small for our instrument to measure. This ionization-induced velocity adds vectorially to the velocity from the C_2 dissociation. The function describing this speed broadening is simply a section of a straight line, with an intensity proportional to the speed, $|\mathbf{v}_{tot}| = |\mathbf{v}_{diss} + \mathbf{v}_{ion}|$. The edges are at $|\mathbf{v}_{diss}| \pm |\mathbf{v}_{ion}|$, and the center is at $\mathbf{v}_{diss}$. This resembles a sloped top hat and is subsequently convolved with a Gaussian line shape to account for the slight transverse velocity spread of the molecular beam and detector response. This Gaussian component was fit to the nozzle-produced carbon peak in the speed distributions and has a full width at half maximum of 15 m·s^{-1}.

The $^3P_0$ distribution in Fig. 3 clearly shows only a single component, modeled very well by our sloped top hat function, resulting from resonant excitation of C_2. The slight tail at high and low velocity underlying the nozzle-produced carbon peak is not modeled well by the single Gaussian, but is shown to be there in the background signal as well (Fig. 2*C*) and is therefore not due to resonant excitation of C_2. The distributions for $^3P_1$ and $^3P_2$ are more complicated. The $^3P_2$ distribution has a shoulder at lower speeds that is not present in the $^3P_0$ distribution, and the $^3P_1$ clearly peaks at higher velocities than $^3P_0$ and $^3P_2$ while also exhibiting a weaker lower-speed component.

Since the relative energies of all possible product states are accurately known (Table 1), the higher-velocity component in the

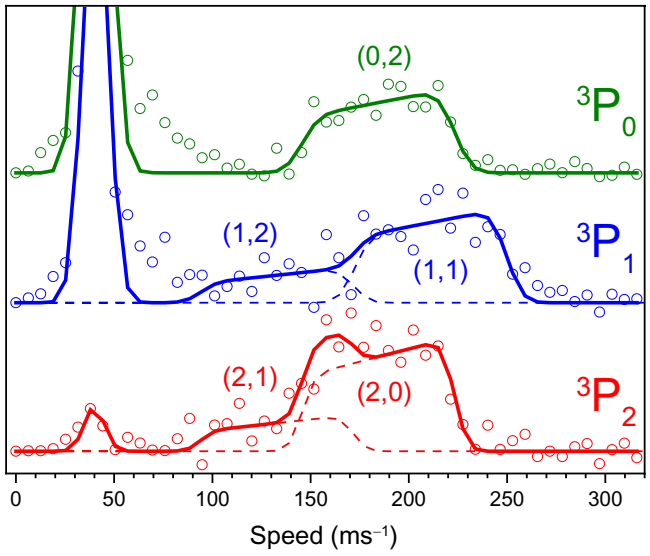

Fig. 3. The three speed distributions in meters per second resulting from the photodissociation of C_2 at 49,864.2 cm^{-1}. The three distributions were measured probing the $^3P_0$ (*Top*, green), $^3P_1$ (*Middle*, blue), and $^3P_2$ (*Bottom*, red) states of carbon, respectively. Open symbols are experimental data points, dashed lines are fitted contributions from the atomic pairs indicated, and solid lines are the sum of these contributions.

$^3P_1$ distribution was readily assigned to a (1,1) pair of carbon atoms, while the shoulders in the $^3P_1$ and $^3P_2$ fit perfectly with a (2,1) pair of atoms. The velocities and total kinetic energy release (TKER: the sum of both carbon kinetic energies) determined for these three exit channels is given in Table 2. There is no evidence of the other carbon atom pairs (0,0), (1,0), and (2,2) in our experimental data. Of these three, the (2,2) product state lies above the excitation energy in our experiment and cannot be seen. The (0,0) and (1,0) would be found at higher speeds than the (2,0) and (1,1) product states, but were not observed (Table 2). The upper molecular state (the F_3 component of $J = 2$) has a total electronic angular momentum of $2\hbar$ projected onto the molecular axis ($\Omega = 2$). This state cannot correlate to the (0,0) and (1,0) pairs, as they have insufficient total electronic angular momentum.

Discussion

With three carbon atom pairs firmly assigned and fitting well to our experimental speed distributions, the dissociation energy of C_2 can readily be determined. The scheme is depicted in Fig. 4. Using the (2,0) pair, the internal energy of the atoms is that of $^3P_2$, that is, 43.41 cm^{-1}. With a kinetic energy release of 34.08 cm^{-1}, this implies our laser excites a level in C_2 at 77.50 cm^{-1} above the minimum energy asymptote, corresponding to the (0,0) atom pair. For the results in Figs. 2*C* and 3, the C_2 excitation laser was set to 49,864.2 cm^{-1}. As the spectrum in Fig. 2 shows, this corresponds to a transition originating from $J = 2$ in the F_1 state of $a^3\Pi_u(v = 0)$. The dissociation energy of C_2 lies,

Table 2. TKER for carbon atom pair states

Product pair (*J*, *J*)	Speed (m·s^{-1})	TKER (cm^{-1})
(2,2)*	–	–9.34†
(2,1)	132.7	17.66
(2,0)	184.3	34.08
(1,1)	211.0	44.66
(1,0)*	246.7	61.07
(0,0)*	277.9	77.49

*Not observed.
†Not accessible.

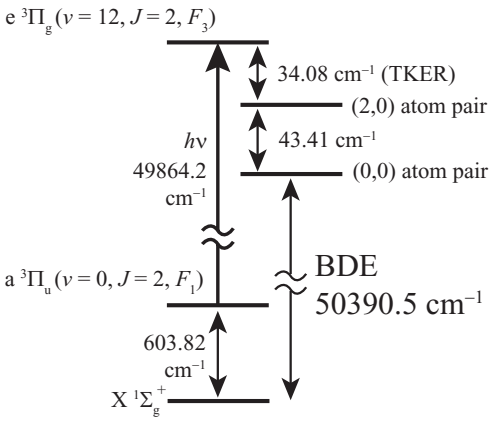

Fig. 4. Determination of the BDE of C_2. The 49,864.2 cm^{-1} photon is absorbed from a state 602.82 cm^{-1} above the absolute ground state. The TKER is measured to be 34.08 cm^{-1}, to atomic states 43.14 cm^{-1} above the atomic ground states. The BDE is determined to be 50,390.5 cm^{-1}.

therefore, 49,864.2 – 77.5 = 49,786.7 cm^{-1} above the energy of $a^3\Pi_u(v = 0, J = 2, F_1)$. The accurate determination of the singlet–triplet gap in C_2 and constants for $X^1\Sigma_g$ and $a^3\Pi_u$ by Chen et al. (36) place the F_1 component of $J = 2$ in $a^3\Pi_u(v = 0)$ at 603.82(3) cm^{-1} above $X^1\Sigma_g$ ($v = 0$). We therefore pinpoint the dissociation energy of C_2 to 50,390.5±2.4 cm^{-1} relative to its ground state (602.804(29) kJ·mol^{-1}).

A high-level ab initio calculation of the BDE of C_2 was also done as part of this study. The procedure followed is similar in spirit to the quite rigorous composite strategies associated with the HEAT (high-accuracy extrapolated ab initio thermochemistry) (37) and Weizmann-n (Wn) (38) families of thermochemical methods but is an elaboration of both made possible by the small size of the target molecule. The strategy employed here is to compute the $a^3\Pi_u$ state of C_2 and the ground state of the carbon atom as accurately as possible, and use the resulting BDE together with the experimentally well-established singlet–triplet energy difference to estimate the BDE of the ground state of C_2. This approach is motivated by the considerably more complicated electronic structure of the $X^1\Sigma_g^+$ state, which has appreciable multireference character and is a much more challenging target for accurate calculation than is the $a^3\Pi_u$ state.

The energies of the atom and the triplet state of C_2 were computed according to a partitioning largely consistent with that used in the HEAT and Wn families of methods. Specifically, the electronic energy was broken into four parts, $E_{\rm elec} = E_{\rm SCF} + E_{\rm CCSD(T)} + (E_{\rm CCSDT} - E_{\rm CCSD(T)}) + E_{\rm HLC}$, where the first two terms are calculated with very large basis sets and then extrapolated to the basis set limit, and the remaining terms—which account for electron correlation effects beyond the well-known coupled-cluster singles and doubles plus perturbative triples [CCSD(T)] approximation—are obtained with feasibly large basis sets in the frozen-core approximation. The final correction attempts to bridge the gap between the full CCSD(T) method and the exact correlation energy ("full configuration interaction"). Beyond this, the energy is augmented by the zero-point correction ($E_{\rm ZPE}$) for C_2, and small corrections for scalar relativity ($E_{\rm SR}$), the difference between the energy of the spin–orbit averaged states that are calculated and the actual lowest spin–orbit sublevels ($E_{\rm SO}$), and the diagonal Born–Oppenheimer correction ($E_{\rm DBOC}$). A full description of this partitioning is given in ref. 38.

The various contributions to the bond energy of the $a^3\Pi_u$ state of C_2 are listed in Table 3, along with details of the basis sets used and the extrapolation procedures. Calculations done in this work differ from the standard HEAT (and Wn) protocols principally in that larger basis sets have been used. The self-consistent field (SCF) and CCSD(T) energies were obtained in all-electron calculations with basis sets up to octuple-zeta quality, the largest of which (aug-cc-pCV7Z and aug-cc-pCV8Z) were those used for the carbon atom in ref. 39. Calculations were done with the CFOUR program suite (40) and the MRCC program (41) that enabled the post-CCSD(T) contributions to $E_{\rm HLC}$.

When augmented by the experimental $X^1\Sigma_g^+/a^3\Pi_u$ splitting of 613.65 cm^{-1} (36), the accumulated result obtained here for the BDE of the triplet state (49,779 cm^{-1}) puts the corresponding theoretical BDE for C_2 at 50,393 cm^{-1} (602.83 kJ·mol^{-1}), which is in excellent agreement with both the experimental number and the earlier calculation of Karton (24) (602.83 kJ·mol^{-1}). It is difficult to estimate the error bar associated with the calculations presented here, but a conservative (2σ) estimate would be 20 cm^{-1}. Nevertheless, the absolute error in both the present calculation and that of Karton is less than 5 cm^{-1}, with both lying just above the precise experimental result.

The ionization energies of C_2 and carbon atoms are accurately known (30, 35). These may be combined with the presently determined BDE(C_2) to obtain BDE(C_2^+) of $45,505 \pm 40$ cm^{-1} (544.36(48) kJ·mol^{-1}). This value compares favorably with the results of high-level ab initio calculations, 45,442 cm^{-1} (42). The $^4\Sigma_g^-$ ground state of the cation has a formal bond order of 1.5. This state is expected to dissociate adiabatically into atoms, and the determined BDE is close to 1.5 times that of a typical C–C single bond. Evidently the bonding in C_2^+ is much simpler to describe than C_2 itself.

To calculate the expected rate of C_2 photodissociation in cometary comae, we calculated the hitherto unobserved vibrational levels of the $e^3\Pi_g$ state at a very high level of ab initio

Table 3. Computed BDE of $a^3\Pi_u$ state C_2

Contribution	Basis sets/procedure	Extrapolation	Value (cm^{-1})
$\Delta E_{\rm SCF}$	aug-cc-pCV*X*Z (*X* = 6, 7, 8)	Exponential*	25,092
$\Delta E_{\rm CCSD(T)}$	aug-cc-pCV*X*Z (*X* = 7, 8)	X^{-3} two-point*	25,181
$\Delta E_{\rm (CCSDT-CCSD(T))}$	cc-pV*X*Z (*X* = 5, 6)	X^{-3} two-point*	–86
$\Delta E_{\rm HLC}$	contributions		
CCSDT(Q)–CCSDT	cc-pV*X*Z (*X* = 4, 5)	X^{-3} two-point*	450
CCSDTQ–CCSDT(Q)	cc-pV*X*Z (*X* = 3)		–20
CCSDTQP–CCSDTQ	cc-pV*X*Z (*X* = 2)		48
CCSDTQPH–CCSDTQP	cc-pV*X*Z (*X* = 2)		3
ZPE	From experimental data		–818
Relativistic	Per HEAT protocol*		–31
SO	From experimental data		–44
DBOC	Per HEAT protocol*		5
Total			49,779

*As described in ref. 37.

quantum mechanical theory. Briefly, the electronic states of C_2 were calculated using multireference configuration interaction with a full-valence complete active space reference state. The aug-cc-pCV6Z basis set was used, and all double excitations out of the reference space, including those from the core, were included. The energies were corrected for higher excitations, by the Davidson correction. All calculations were undertaken with the Molpro package (43). Energy levels were obtained by solving the vibrational Schrödinger equation on spline-interpolated potential energy curves. The resulting origin band of the Fox–Herzberg system was calculated to be at 39,698 cm^{-1}, to be compared with the experimental value of 39,806.8 cm^{-1} (25). Up to $v = 12$, the calculated levels were found to deviate approximately linearly from experiment, and, after applying this small linear correction, the mean absolute deviation between modeled and experimental band positions was 0.6 cm^{-1}. This correction was applied to the predissociated levels, $v' \geq 12$. We computed up to $v' = 32$, and confirmed the predissociated nature of the levels using a diabatic approach.

In the diabatic approach, the global electronic structure of the $C_2\,{}^3\Pi_g$ states, up to the $2s^22p^2$ (^3P) + $2s2p^3$ (^5S) dissociation channel, is modeled using the diabatic state interaction picture. The diabatization scheme involves curve crossings between a deeply bound diabatic state with several other weakly bound or repulsive states. A fit model, based on this scheme, reproduces the energy levels from all four observed $^3\Pi_g$ electronic states ($v = 0$ to 12 of $d^3\Pi_g$ and $e^3\Pi_g$, and five v levels of the coupled $3,4^3\Pi_g$ states) with an average fit residual of ∼0.4 cm^{-1}. Based on this fit model, the predissociation lifetimes of the $e^3\Pi_g$ state levels are all found to be < 100 ps, which is significantly shorter than the expected $e^3\Pi_g$ state radiative decay lifetime (∼400 ns; *SI Appendix*). Details of this diabatic model will be reported in a future publication (see *SI Appendix* for brief description).

The $a^3\Pi_u$ state levels were taken from ref. 44, but the quality of the calculations is evidenced by a mean absolute deviation between observed and calculated vibrational levels of only 0.9 cm^{-1} up to $v = 9$.

The transition dipole moments, μ_{ji}, were calculated, and the excitation rates k_{ji} were obtained from

$$k_{ji} = B^f_{ji}\rho^f(f_{ji}), \qquad [1]$$

where (45)

$$B^f_{ji} = \frac{\mu^2_{ji}}{6\varepsilon_0\hbar^2}, \qquad [2]$$

and $\rho^f(f_{ji})$ is the solar spectral energy density in joules per cubic meter per hertz at frequency $f_{ji} = c/\lambda_{ji}$ (46). To obtain the total dissociation rate, individual rates are weighted by the occupancies of the lower levels, i. These comprise two factors, an effective vibrational temperature and the ratio of $a^3\Pi_u$ to $X^1\Sigma^+_g$ C_2 molecules. The effective vibrational temperature is taken to be 5,500 K (47). If the proportion of molecules in the triplet manifold is p_a, then the dissociation rate may be written as

$$k_{diss} = p_a \frac{\sum_{j\geq 12, i\leq 9} k_{ji}\exp(-E_i/5500k_B)}{\sum_{i\leq 9}\exp(-E_i/5500k_B)} \qquad [3]$$

$$= 6.7\times 10^{-6}\mathrm{s}^{-1}p_a. \qquad [4]$$

The upper state level, j, was limited to $12 \leq v' \leq 32$. The uncertainty in this truncation is much less than other sources of uncertainty. The lifetime of $a^3\Pi_u$ state C_2 is thus calculated to be 1.5×10^5 s, notwithstanding other unknown photodissociation processes.

The relative population of triplet and singlet C_2 depends crucially on the strength of intercombination transitions. Indeed, this is how C_2 cools in space (48, 49). Having no permanent dipole moment, it is unable to radiate efficiently through rotational transitions, and, being a homonuclear diatomic molecule, possesses no pure vibrational spectrum. Spin–orbit coupling mixes the ground $X^1\Sigma^+_g$ and excited $b^3\Sigma^-_g$ states, and thus excited vibrational levels in the $X^1\Sigma^+_g$ state can radiate to the $a^3\Pi_u$ state by borrowing intensity from the Ballik–Ramsay (50) system. The $a^3\Pi_u$ state levels may radiate to lower-lying $X^1\Sigma^+_g$ state levels by the same mechanism.

The singlet–triplet ratio can be inferred from observations of the relative fluxes in emission due to singlet and triplet band systems in cometary spectra. A'Hearn and Feldman (51) observed the $D^1\Sigma^+_u \rightarrow X^1\Sigma^+_g$ Mulliken emission in comet Bradfield 1979l. The interpolated flux ratio $F(\mathrm{Mulliken})/F(\mathrm{Swan}) \approx 2.2\times 10^{-3}$ implies a population ratio of $N_S/N_T \approx 0.7$ from the g factors that relate molecular abundances to observed fluxes (22, 51). As such, the fraction of $a^3\Pi_u$ state is about 0.59, and the dissociation rate of cometary C_2 due to the predissociated Fox–Herzberg system is 3.9×10^{-6} s^{-1} at 1 AU.

The ionization rate of $X^1\Sigma^+_g$ state C_2 at 1 AU was estimated by Huebner et al. (52) to be about 1×10^{-6} s^{-1}. But calculations by Toffoli and Lucchese (53) put the $a^{+2}\Pi_u \leftarrow X^1\Sigma_g$ ionization cross-section near threshold to be 50 Mb, halving for each additional 10 eV. Taking this function with the solar spectrum in ref. 46, we obtain an ionization rate for the ground state of 4.0×10^{-6} s^{-1}. A similar calculation for the $X^{+4}\Sigma^-_g \leftarrow a^3\Pi_u$ process ($\sigma_{\mathrm{thresh.}} \approx 10$ Mb) results in an ionization rate of 1.0×10^{-6} s^{-1}. Combining these ionization rates with the above $a^3\Pi_u$ photodissociation rate and the small contribution from $X^1\Sigma^+_g$ photodissociation (52, 54), we obtain a total photodestruction rate of 6.2×10^{-6} s^{-1}, corresponding to a lifetime of 1.6×10^5 s (2 d) at 1 AU. The contributions to this rate are summarized in Table 4.

In an analysis of comets Tuttle 1980h and Meier 1980q, Cochran (21) estimated the photodissociation rate of C_2 to be 4×10^{-6} s^{-1}, which is clearly in agreement with the present estimation. However, the lifetime of cometary C_2 cannot be measured directly. It is inferred from the observed spatial distribution in the coma and the outflow velocity. The spatial distribution of C_2 in the coma is typically analyzed with the Haser model (55, 56). The Haser model assumes a spherically symmetric outflow at a constant velocity. Species can be emitted directly from the nucleus or generated photolytically from parent species (58). In the case of C_2, it is usually fit as a so-called daughter product, although the parentage is complicated (21, 57, 59).

A set of measurements on Comet P/Halley determined a scale length for C_2 of $5.76(45)\times 10^4$ km (60). A very similar number was reported by Nelson et al. (47) for Comet 122P/de Vico. A summary of scale lengths for various comets are given in ref. 57. While there is some variation, the C_2 scale lengths are typically of the order 6×10^4 km. If the parent or grandparent of C_2 is an organic grain, an outflow velocity of about 0.5 km·s^{-1} is expected. This results in a lifetime of 1.2×10^5 s at 1 AU, which is about 0.7 of that determined above. Recently, Pierce and Cochran (61) reported the spatial analysis of four comets using an integral field spectrograph. They adopted a scale length for C_2 of 120,000 km, with an outflow velocity at 1 AU of 0.85 km·s^{-1}. Their derived lifetime is 1.4×10^5 s.

What is clear is that the observations are consistent with the presently proposed mechanism being a significant contributor to the cometary photodissociation of C_2. While it is ultimately a

Table 4. Rates of photoprocesses of C_2 at 1 AU

		Rate (10^{-6} s^{-1})		
State	Fraction	k_{diss}	k_{ion}	Contribution
$X^1\Sigma^+_g$	0.411	0.1	4.0	1.7
$a^3\Pi_u$	0.589	6.7	1.0	4.5
Total	1.000			6.2

one-photon process from the $a^3\Pi_u$ state, it takes several steps (minimum) for a ground-state $X^1\Sigma_g^+$ molecule to have its bonds unpicked: 1) absorption $A^1\Pi_u \leftarrow X^1\Sigma_g^+$, 2) emission $A^1\Pi_u \rightarrow X^1\Sigma_g^+(v>0)$, 3) intercombination emission $X^1\Sigma_g^+(v>0) \rightarrow a^3\Pi_u$, 4) absorption $e^3\Pi_g \leftarrow a^3\Pi_u$, 5) curve-crossing $e^3\Pi_g \rightarrow d^3\Pi_g$, and 6) dissociation $C_2 \rightarrow C(^3P) + C(^3P)$.

Whether or not one accepts that C_2 has a quadruple bond (2), its route from the ground state to dissociation in a cometary environment involves more than one photon, and breaks two spectroscopic rules along the way: spin conservation and the Born–Oppenheimer approximation. Our discovery of this mechanism would not have been possible without the thorough exploration of the ultraviolet spectroscopy of C_2 (25, 28, 29, 31), highlighting that laboratory studies are required to rigorously explain astronomical phenomena.

Conclusions

We have employed velocity-map imaging (VMI) and multiphoton ionization to observe the photodissociation of C_2. It dissociates through predissociation of the $e^3\Pi_g$ state at high vibrational levels (31), as predicted by Herzberg (20). From careful analysis of the images, we determined a BDE of $50{,}390.5 \pm 2.4$ cm^{-1}, bringing the precision into line with other homonuclear diatomics. The value agrees very well with the best possible calculations. Assuming near-unity dissociation yield for $e^3\Pi_g(v \geq 12)$, we calculate a lifetime for cometary C_2 of about 1.6×10^5 s, which is consistent with cometary observations. This process explains the mechanism for cometary C_2 photodissociation, which ultimately explains why it is that the coma of a comet is often green, but its tail is not.

Experimental Methods. The VMI apparatus itself has been described previously (62). Three lasers were used for this experiment. In brief, C_2 was generated by photolysis of precursor C_2Cl_4 (0.8% in 3-bar helium) in the expansion region of a supersonic molecular beam. The photolysis laser, 0.5 mJ to 1 mJ per pulse of 209.5 nm light (doubled Exalite 417 from a Quanta-Ray Pro-230 pumped Cobra Stretch dye laser, pulse duration ∼5 ns), was focused by a 450-mm-focal-length lens ∼1 mm in front of the nozzle orifice to optimally produce C_2 in $a^3\Pi_u$ $(v=0)$ and in low rotational levels; 209.5 nm is near the peak of the C_2Cl_4 absorption spectrum, which allowed us to keep the photolysis laser power low. Further information on this process is available in *SI Appendix*. Post skimmer and between the VMI repeller and extractor electrodes, C_2 was excited to $v=12$ in the $e^3\Pi_g$ state using the frequency-tripled output from a second Quanta-Ray-pumped Cobra Stretch dye laser operating on a Rhodamine 610/640 mixture. The pulse energy was kept to below 0.4 mJ (5-ns pulse width). The beam was unfocused and irised to a beam diameter of around 1 mm. This was done to minimize multiphoton effects and background signals from photolysis of the remaining tetrachloroethylene precursor.

Carbon atoms were probed by (2+1) REMPI at 280 nm, produced as the doubled output of a Lambda-Physik dye laser operating with Rhodamine 6G laser dye. Typical C-REMPI laser powers were 0.7 mJ per pulse to 1 mJ per pulse, 5 to 10 ns pulse width. The entire experiment was run at a repetition rate of 20 Hz. The second ("pump") and third ("probe") lasers were counterpropagating perpendicular to the molecular beam, overlapped spatially, and timed to be 40 ns apart. Both lasers were vertically polarized. At the atomic speeds detected, we expect Doppler shifts of just 0.04 cm^{-1}, which is much less than the ∼0.1 cm^{-1} laser line width.

To resolve the low-speed carbon images, the VMI extraction voltages were lowered by a factor of 4 from what they normally operate at, allowing for an additional magnification of the image by a factor of 2. These new extraction conditions were characterized using the well-known multiphoton excitation of O_2 around 225 nm (63). VMI conditions were confirmed by verifying that the O_2^+ parent ion signal illuminated a single pixel with no contamination from spatial mapping, and the radius-to-velocity calibration was determined by analyzing the kinetic energy distribution of O^+ ions. The wavelengths of the three lasers were checked by a Toptica HighFinesse WS5 Wavelength Meter with an accuracy better than 0.001 nm, which translates to < 0.1 cm^{-1} for the C_2 excitation laser.

Data Availability. All study data are included in the article and/or *SI Appendix*.

ACKNOWLEDGMENTS. This work was supported by the Australian Research Council (grant DP190103151). It was undertaken with the assistance of resources from the National Computational Infrastructure, which is supported by the Australian Government (Project zu57, Centre of Excellence in Exciton Science, grant CE170100026). J.J. assisted in the preparation of this manuscript at the Lawrence Livermore National Laboratory under the auspices of the US Department of Energy by Lawrence Livermore National Laboratory under Contract DE-AC52-07NA27344.

1. T. W. Schmidt, The spectroscopy of C_2: A cosmic beacon. *Acc. Chem. Res.* **54**, 481–489 (2021).
2. S. Shaik *et al.*, Quadruple bonding in C_2 and analogous eight-valence electron species. *Nat. Chem.* **4**, 195–200 (2012).
3. S. Shaik, H. S. Rzepa, R. Hoffmann, One molecule, two atoms, three views, four bonds? *Angew. Chem. Int. Ed. Engl.* **52**, 3020–3033 (2013).
4. D. Danovich, P. C. Hiberty, W. Wu, H. S. Rzepa, S. Shaik, The nature of the fourth bond in the ground state of C_2: The quadruple bond conundrum. *Chemistry* **20**, 6220–6232 (2014).
5. W. Heitler, F. London, Wechselwirkung neutraler atome und homöopolare bindung nach der quantenmechanik [in German]. *Z. Phys.* **44**, 455–472 (1927).
6. G. Frenking, M. Hermann, Critical comments on "One molecule, two atoms, three views, four bonds?" *Angew. Chem. Int. Ed. Engl.* **52**, 5922–5925 (2013).
7. D. Danovich, S. Shaik, H. S. Rzepa, R. Hoffmann, A response to the critical comments on "One molecule, two atoms, three views, four bonds?" *Angew. Chem. Int. Ed. Engl.* **52**, 5926–5928 (2013).
8. S. Shaik, D. Danovich, B. Braida, P. C. Hiberty, The quadruple bonding in C_2 reproduces the properties of the molecule. *Chemistry* **22**, 4116–4128 (2016).
9. G. Frenking, M. Hermann, Comment on "the quadruple bonding in C_2 reproduces the properties of the molecule." *Chemistry* **22**, 18975–18976 (2016).
10. M. Hermann, G. Frenking, The chemical bond in C_2. *Chemistry* **22**, 4100–4108 (2016).
11. Y. Liu, T. J. Frankcombe, T. W. Schmidt, Chemical bonding motifs from a tiling of the many-electron wavefunction. *Phys. Chem. Chem. Phys.* **18**, 13385–13394 (2016).
12. F. Querci, M. Querci, T. Tsuji, Model atmospheres for C type stars. *Astron. Astrophys.* **31**, 265–282 (1974).
13. D. Goorvitch, The C_2 Ballik-Ramsay transitions in carbon stars. *Astrophys. J. Suppl. Ser.* **74**, 769–783 (1990).
14. S. P. Souza, B. L. Lutz, Detection of C_2 in the interstellar spectrum of Cygnus OB2 Number 12 (VI Cygni Number 12). *Astrophys. J.* **216**, L49–L51 (1977).
15. D. L. Lambert, Y. Sheffer, S. R. Federman, Hubble Space Telescope observations of C_2 molecules in diffuse interstellar clouds. *Astrophys. J.* **438**, 740–749 (1995).
16. M. Köhler, A. Brockhinke, M. Braun-Unkhoff, K. Kohse-Höinghaus, Quantitative laser diagnostic and modeling study of C_2 and CH chemistry in combustion. *J. Phys. Chem. A* **114**, 4719–4734 (2010).
17. W. H. Wollaston, A method of examining refractive and dispersive powers, by prismatic reflection. *Philos. Trans. R. Soc. Lond. B Biol. Sci.* **92**, 365–380 (1802).
18. W. Swan, On the prismatic spectra of the flames of compounds of carbon and hydrogen. *Proc. R. Soc. Edinb.* **3**, 376–377 (1857).
19. W. Huggins, On the spectrum of comet II, 1868. *Proc. R. Soc. Lond.* **16**, 481–482 (1868).
20. G. Herzberg, Dissociation, predissociation, and recombination of diatomic molecules. *Astrophys. J.* **89**, 290–292 (1939).
21. A. L. Cochran, C_2 photolytic processes in cometary comae. *Astrophys. J.* **289**, 388–391 (1985).
22. M. F. A'Hearn, R. C. Millis, D. G. Schleicher, D. J. Osip, P. V. Birch, The ensemble properties of comets: Results from narrowband photometry of 85 comets, 1976-1992. *Icarus* **118**, 223–270 (1995).
23. B. Ruscic, D. H. Bross, Active thermochemical tables (ATcT) values based on ver. 1.122p of the thermochemical network. https://atct.anl.gov/Thermochemical%20Data/version%201.122p/. Accessed 14 October 2021.
24. A. Karton, Basis set convergence of high-order coupled cluster methods up to CCSDTQ567 for a highly multireference molecule. *Chem. Phys. Lett.* **737**, 136810 (2019).
25. B. A. Welsh *et al.*, The $e^3\Pi_g$ state of C_2: A pathway to dissociation. *J. Chem. Phys.* **147**, 024305 (2017).
26. D. L. Kokkin *et al.*, Observation of the $d^3\Pi_g \leftarrow c^3\Sigma_u^+$ band system of C_2. *J. Chem. Phys.* **125**, 231101 (2006).
27. J. A. Joester *et al.*, The $d^3\Pi_g$-$c^3\Sigma_u^+$ band system of C_2. *J. Chem. Phys.* **127**, 214303 (2007).
28. O. Krechkivska *et al.*, First observation of the $3^3\Pi_g$ state of C_2: Born-Oppenheimer breakdown. *J. Chem. Phys.* **146**, 134306 (2017).

29. O. Krechkivska *et al.*, Resonance-enhanced 2-photon ionization scheme for C_2through a newly identified band system: $4^3\Pi_g$-$a^3\Pi_u$. *J. Phys. Chem. A* **119**, 12102–12108 (2015).
30. O. Krechkivska *et al.*, The ionization energy of C_2. *J. Chem. Phys.* **144**, 144305 (2016).
31. O. Krechkivska *et al.*, Higher vibrational levels of the $D^1\Sigma_u^+$ state of dicarbon: New Mulliken bands. *J. Mol. Spectrosc.* **344**, 1–5 (2018).
32. C. Huang *et al.*, Kinetics of C_2 ($a^3\Pi_u$) radical reactions with alkanes by LIF. *J. Chem. Phys.* **120**, 2225–2229 (2004).
33. R. L. Whetten, K. J. Fu, R. S. Tapper, E. R. Grant, Highly efficient production of neutral carbon-atoms in the ultraviolet multiphoton fragmentation of aromatic-molecules. *J. Phys. Chem.* **87**, 1484–1487 (1983).
34. D. D. Hickstein, S. T. Gibson, R. Yurchak, D. D. Das, M. Ryazanov, A direct comparison of high-speed methods for the numerical Abel transform. *Rev. Sci. Inst.* **90**, 065115 (2019).
35. K. Haris, A. Kramida, Critically evaluated spectral data for neutral carbon (C I). *Astrophys. J. Supp. Ser.* **233**, 16 (2017).
36. W. Chen, K. Kawaguchi, P. F. Bernath, J. Tang, Simultaneous analysis of the Ballik-Ramsay and Phillips systems of C_2 and observation of forbidden transitions between singlet and triplet states. *J. Chem. Phys.* **142**, 064317 (2015).
37. A. Tajti *et al.*, HEAT: High accuracy extrapolated ab initio thermochemistry. *J. Chem. Phys.* **121**, 11599–11613 (2004).
38. A. Karton, E. Rabinovich, J. M. L. Martin, B. Ruscic, W4 theory for computational thermochemistry: In pursuit of confident sub-kJ/mol predictions. *J. Chem. Phys.* **125**, 144108 (2006).
39. N. Dattani, G. LiManni, D. Feller, J. Koput, Computer-predicted ionization energy of carbon within 1 cm^{-1} of the best experiment. arXiv [Preprint] (2020). https://arxiv.org/abs/2006.13453 (Accessed 14 October 2021).
40. D. A. Matthews *et al.*, Coupled-cluster techniques for computational chemistry: The CFOUR program package. *J. Chem. Phys.* **152**, 214108 (2020).
41. M. Kállay *et al.*, The MRCC program system: Accurate quantum chemistry from water to proteins. *J. Chem. Phys.* **152**, 074107 (2020).
42. D. Shi, X. Niu, J. Sun, Z. Zhu, Potential energy curves, spectroscopic parameters, and spin–orbit coupling: A theoretical study on 24 Λ-S and 54 Ω states of C_2^+ cation. *J. Phys. Chem. A* **117**, 2020–2034 (2013).
43. H. J. Werner *et al.*, The Molpro quantum chemistry package. *J. Chem. Phys.* **152**, 144107 (2020).
44. J. S. Brooke, P. F. Bernath, T. W. Schmidt, G. B. Bacskay, Line strengths and updated molecular constants for the C_2 swan system. *J. Quant. Spectrosc. Radiat. Transf.* **124**, 11–20 (2013).
45. R. C. Hilborn, Einstein coefficients, cross sections, f values, dipole moments, and all that. *Am. J. Phys.* **50**, 982–986 (1982).
46. C. A. Gueymard, Revised composite extraterrestrial spectrum based on recent solar irradiance observations. *Sol. Energy* **169**, 434–440 (2018).
47. T. Nelson, A. L. Cochran, C. Western, Rotational temperature modeling of the Swan $\Delta v = 0$ band sequence in comet 122p/de Vico. *J. Phys. Chem. A* **122**, 8020–8025 (2018).
48. R. Gredel, E. F. van Dishoeck, J. H. Black, Fluorescent vibration-rotation excitation of cometary C_2. *Astrophys. J.* **338**, 1047 (1989).
49. E. F. van Dishoeck, J. H. Black, The excitation of interstellar C_2. *Astrophys. J.* **258**, 533–547 (1982).
50. E. A. Ballik, D. A. Ramsay, Infrared emission spectra from a carbon furnace. *J. Chem. Phys.* **29**, 1418–1419 (1958).
51. M. F. A'Hearn, P. D. Feldman, Carbon in Comet Bradfield 1979l. *Astrophys. J.* **242**, L187–L190 (1980).
52. W. F. Huebner, J. J. Keady, S. P. Lyon, Solar photo rates for planetary atmospheres and atmospheric pollutants. *Astrophys. Space Sci.* **195**, 1–294 (1992).
53. D. Toffoli, R. R. Lucchese, Near threshold photoionization of the ground and first excited states of C_2. *J. Chem. Phys.* **120**, 6010–6018 (2004).
54. B. Pouilly, J. M. Robbe, J. Schamps, E. Roueff, Photodissociation and radiative processes in interstellar C_2. *J. Phys. B* **16**, 437–448 (1983).
55. L. Haser, S. Oset, D. Bodewits, Intensity distribution in the heads of comets. *Planet. Sci. J.* **1**, 83 (2020).
56. L. Haser, Distribution d'intensit'e dans la tête d'une comète [in French]. *Bull. Cl. Sci. Acad. R. Belg.* **43**, 740–750 (1957).
57. M. R. Combi, U. Fink, A critical study of molecular photodissociation and CHON grain sources for cometary C_2. *Astrophys. J.* **484**, 879–890 (1997).
58. W. M. Jackson, Y. Bao, R. S. Urdahl, Implications of C_2H photochemistry on the modeling of C_2 distributions in comets. *J. Geophys. Res.* **96**, 17569–17572 (1991).
59. P. Rousselot, J. Clairemidi, G. Moreels, Evolution of the C_2 spectrum in Halley's inner coma: Evidence for a diffuse source. *Astron. Astrophys.* **286**, 645–653 (1994).
60. U. Fink, M. R. Combi, M. A. Disanti, Comet P/Halley: Spatial distributions and scale lengths for C_2, CN, NH_2, and H_2O. *Astrophys. J.* **383**, 356 (1991).
61. D. M. Pierce, A. L. Cochran, Examination of fragment species in the comae of several comets using an integral field unit spectrograph. *Planet. Sci. J.* **2**, 19 (2021).
62. N. Hobday *et al.*, Experimental and theoretical investigation of triple fragmentation in the photodissociation dynamics of H_2CO. *J. Phys. Chem. A* **117**, 12091–12103 (2013).
63. A. T. J. B. Eppink, D. H. Parker, Velocity map imaging of ions and electrons using electrostatic lenses: Application in photoelectron and photofragment ion imaging of molecular oxygen. *Rev. Sci. Instrum.* **68**, 3477–3484 (1997).